UNIVERSITY OF AMSTERDAM

UvA-DARE (Digital Academic Repository)

Primary Fibril Nucleation of Aggregation Prone Tau Fragments PHF6 and PHF6*

Smit, F.X.; Luiken, J.A.; Bolhuis, P.G.

DOI
10.1021/acs.jpcb.6b07045

Publication date
2017

Document Version
Final published version

Published in
The journal of Physical Chemistry. B

License
Article 25fa Dutch Copyright Act (https://www.openaccess.nl/en/policies/open-access-in-dutch-copyright-law-taverne-amendment)

Link to publication

Citation for published version (APA):
Smit, F. X., Luiken, J. A., & Bolhuis, P. G. (2017). Primary Fibril Nucleation of Aggregation Prone Tau Fragments *PHF6* and *PHF6**. *The journal of Physical Chemistry. B*, *121*(15), 3250-3261. https://doi.org/10.1021/acs.jpcb.6b07045

General rights
It is not permitted to download or to forward/distribute the text or part of it without the consent of the author(s) and/or copyright holder(s), other than for strictly personal, individual use, unless the work is under an open content license (like Creative Commons).

Disclaimer/Complaints regulations
If you believe that digital publication of certain material infringes any of your rights or (privacy) interests, please let the Library know, stating your reasons. In case of a legitimate complaint, the Library will make the material inaccessible and/or remove it from the website. Please Ask the Library: https://uba.uva.nl/en/contact, or a letter to: Library of the University of Amsterdam, Secretariat, P.O. Box 19185, 1000 GD Amsterdam, The Netherlands. You will be contacted as soon as possible.
UvA-DARE is a service provided by the library of the University of Amsterdam (https://dare.uva.nl)

Download date:11 Oct 2026

THE JOURNAL OF PHYSICAL CHEMISTRY B

Article

pubs.acs.org/JPCB

Primary Fibril Nucleation of Aggregation Prone Tau Fragments *PHF6* and *PHF6**

Florent X. Smit, Jurriaan A. Luiken, and Peter G. Bolhuis*

van't Hoff Institute for Molecular Sciences, University of Amsterdam, PO Box 94157, 1090 GD Amsterdam, The Netherlands

ABSTRACT: We performed replica exchange molecular dynamics and forward flux sampling simulations of hexapeptide VQIINK and VQIVYK systems, also known as, respectively, fragments *PHF6** and *PHF6* from the tau protein. Being a part of the microtubule binding region, these fragments are known to be aggregation prone, and at least one of them is a prerequisite for fibril formation of the tau protein. Using a coarse-grained force field, we establish the phase behavior of both fragments, and investigate the nucleation kinetics for the conversion into a β-sheet fibril. As the conversion is, in principle, a reversible process, we predict the rate constants for both the fibril formation and melting, and examine the corresponding mechanisms. Our simulations indicate that, while both fragments form disordered aggregates, only *PHF6* is able to form β-sheet fibrils. This observation provides a possible explanation for the lack of available steric zipper crystal structures for *PHF6**.

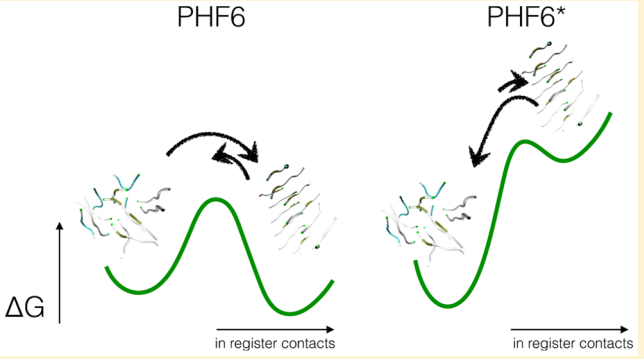

Downloaded via UNIV AMSTERDAM on September 10, 2018 at 09:23:08 (UTC).
See https://pubs.acs.org/sharingguidelines for options on how to legitimately share published articles.

INTRODUCTION

Microtubule associated protein tau (MAPT), also known as *tau*, is a natively unfolded protein[1,2] involved in the regulation of microtubule stability and therefore indirectly in the regulation of intracellular microtubule networks in the central nervous system.[3−6] A repeat sequence, known as the microtubule binding region (MTBR), along with the neighboring proline-rich domain enables binding to microtubules.[2,7−9] While *tau* is largely hydrophilic in nature and soluble, hydrophobic motifs in the MTBRs allow *tau* to form strong bonds with side chains of tubulin, resulting in an increased stability of the microtubule. Phosphorylation of *tau* lowers its affinity to bind to microtubules and therefore results in a loss of stability and rigidity, while *vice versa* microtubule stabilization occurs due to (partial) dephosphorylation of *tau*. While most tauopathies are due to mutations,[10] hyperphosphorylation of *tau* is observed in many forms of dementia, causing a dramatic decrease in its binding affinity to microtubules.[11,12] As a consequence, the resulting pool of dissociated *tau* assembles into β-like structures driven by hydrophobic interactions between the exposed MTBRs.[13] First, dimers and small soluble oligomers form, which on their own display only little toxicity.[14] As stacking continues, however, bundles of *tau* interact and settle into coiled-coil-like structures, so-called paired helical filaments (PHFs), with widths varying between 10 and 20 nm.[15] Eventually, PHFs stick together, forming neurofibrilary tangles (NFT), one of the distinctive hallmarks of Alzheimer's disease.[16,17] However, while the extent of neurodegeneration correlates with the presence of NFTs, it is still not clear what specific process results in its neuronal toxicity and whether NFTs play a leading role in this mechanism. Gaining an understanding of *tau*−*tau* interplay and apprehending the properties resulting in *tau* assembly might lead to insights which can be used for the prevention of *tau*-induced toxicity in Alzheimer's and other tauopathies.

Previous research highlights two particular fragments, VQIINK and VQIVYK in the MTBR repeats, respectively, called *PHF6** and *PHF6*, as key sequences in *tau* fibrilization and assembly[18] (see Figure 1). It is suggested that these motifs are notably prone to aggregate and that at least one of these hexapeptide sequences is a prerequisite for *tau* oligomer formation.[19] Remarkably, only *PHF6* seems to have an available steric zipper crystal structure. In 2001, Bergen et al. proposed two sequences containing these fragments as a subject for the study of *tau* assembly, *R2/wt* and *R3/wt*, which can be used to determine the effect that the *PHF* fragments have as part of a larger whole.[20]

Molecular simulation can complement experimental work by giving detailed mechanistic insight into the aggregation process. However, simulations are hampered by several obstacles. First, system sizes are large, making the use of explicit force fields expensive. Second, the force fields themselves are not well suited for intrinsically disordered proteins. Third, the process of aggregation and fibrilization is a rare event that takes place on the minute to hour time scale *in vitro* and on the year time scale *in vivo*. Clearly, this puts stringent limitations on a straightforward all-atom approach.

Special Issue: Klaus Schulten Memorial Issue

Received: July 14, 2016
Revised: October 23, 2016
Published: October 24, 2016

© 2016 American Chemical Society

DOI: 10.1021/acs.jpcb.6b07045
J. Phys. Chem. B 2017, 121, 3250−3261

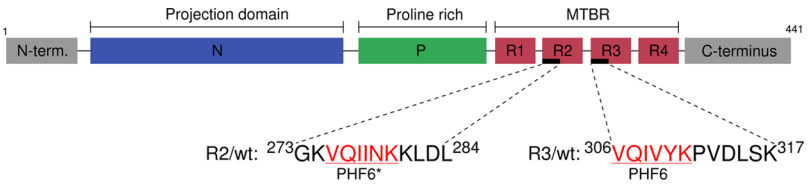

Figure 1. Schematic representation of (one of the isoforms of) *tau* with the locations of *R2/wt*, *R3/wt*, *PHF6*, and *PHF6** indicated. Note that *PHF6** and *R2/wt* do not occur in all isoforms.[11]

In a recent simulation study employing replica exchange molecular dynamics,[21] it was revealed that both *R2/wt* and *R3/wt* have the tendency to dimerize: the first step toward aggregation. In this work, we focus on the primary nucleation kinetics of the short hexapeptides, *PHF6** and *PHF6*, which play a large role in the aggregation of *tau*. Hydrophobic peptides are known to fibrilize via a two-step nucleation mechanism, in which the peptide first forms disordered oligomers after which the oligomers can rearrange themselves into an ordered β-sheet.[22,23] The disordered oligomer to β-sheet fibril is in principle an activated process, especially when near the coexistence conditions. Previous work employing straightforward MD showed spontaneous oligomerization and some signs of β-sheet formation but never a full reorganization into a full fibril structure.[24] By performing Monte Carlo simulations using an all-atom implicit solvent model, Li et al.[25] were able to observe fibril nucleation and growth. Still, slow aggregation processes cannot easily be studied with straightforward explicit solvent all-atom simulations. Therefore, a wide range of coarse-grained force fields was developed to study peptide aggregation (for a review, see ref 26). Besides his seminal work in theoretical and computational biophysics, Klaus Schulten has more recently also made a substantial contribution to this research area with the PACE hybrid force field.[27,28] In this work, we apply the midresolution coarse-grained force field parametrized for peptide folding and aggregation by Bereau and Deserno.[29] While fibril formation of *PHF6* has been observed using coarse-grained force fields,[30] it remains in principle a rare event due to the presence of nucleation barriers. To overcome the nucleation barrier toward fibril formation, we make use of rare event methods, in particular replica exchange molecular dynamics (REMD) and forward flux sampling (FFS). As fibril formation is in first instance driven by thermodynamic forces, and only in second instance controlled by kinetics, it makes sense to establish the thermodynamics of the system with REMD prior to studying the kinetics with FFS.

The paper is organized as follows. After reviewing the employed methodology, we report on the equilibrium phase behavior of the peptide systems. First, we compare the dimerization properties of *PHF6** and *PHF6*. Next, we move to larger system sizes and establish that, while *PHF6* forms β-sheet fibrils, *PHF6** does not. Finally, we focus on the kinetics and mechanism of fibril formation for temperatures not too far from coexistence, where the barrier to nucleation is substantial. We analyze the mechanisms, rates, and free energy landscapes, and indeed conclude that the *PHF6** peptide does not fibrilize at the studied temperatures. In the Discussion section, we provide an explanation for this finding. We end with concluding remarks.

METHODS

Force Field and Simulation Engine. We used the generic midresolution coarse-grained (CG) peptideB model developed by Bereau and Deserno,[29] which offers full sequence specificity. As this force field includes backbone hydrogen bonds, it has proven to be particularly accurate compared to other coarse-grained force fields when it comes to the prediction of the secondary structure of proteins. The model is parametrized such that both α-helical and β-sheet structures are equally accessible, which makes it more generic and realistic. This is partly achieved by including dipole interactions between carbonyl and amide groups. The solvent is treated implicitly in this model. For a detailed description of the model, we refer to ref 29. The integration was carried out by the ESPResSo[31,32] MD package using Langevin dynamics with a 2 fs time step and a friction coefficient of 1.0 ps^{-1}. All MD snapshots were made with VMD.[33]

REMD Simulation. Replica exchange molecular dynamics (REMD) simulates multiple system copies in parallel at different temperatures. Exchanging temperatures between replicas using a Monte Carlo algorithm allows these replicas to diffuse in temperature space, which can dramatically enhance sampling for complex systems with large free energy barriers.[34] To determine the temperature range used for the REMD simulations, a trial simulation was initiated with a geometrical temperature distribution, after which we determined a theoretical exchange probability and calculated an optimized temperature distribution.[35] This step is especially important when a (pseudo) phase transition is present, as the energy fluctuations at the phase transition prevent proper mixing of the replicas.

For the *PHF6** and *PHF6* dimerization, two fragments were positioned in a cubic box with edges of 51 Å, resulting in an overall concentration of 25 mM. REMD was performed using a temperature range of 210−518 K. The systems were simulated for 400 ns preceded by 100 ns equilibration, swapping replicas every 10 ps with an average exchange probability of ∼30%.

To study aggregation of more than two peptides, we initialized three systems with $N \in \{8, 12, 20\}$ peptides in a box with edges of 81 Å for $N = 8$ and 102 Å for both $N = 12$ and $N = 20$, corresponding to concentrations between 20 and 30 mM. REMD was performed with a temperature range of 210 to ∼470 K in all cases. $N = 8$ and $N = 12$ were simulated for 900 ns, with an exchange of replicas every 20 ps, while $N = 20$ was simulated for 400 ns and exchanged replicas every 10 ps. All simulations were preceded by 100 ns equilibration and presented an exchange probability between 20 and 30%. The replica flow, $f(T_i)$, defines the capability of a system to move through temperature space and is defined as the fraction of replicas that diffused from the lowest to the highest temperature versus the temperature index i.[35]

Cluster analysis of these coarse-grained REMD simulations was in part carried out using home-written scripts.[36] A peptide

DOI: 10.1021/acs.jpcb.6b07045
J. Phys. Chem. B 2017, 121, 3250−3261

is part of a (fibrillar) cluster when four to six of its C_α atoms are within 6.5 Å of the matching atom of any another peptide. The average interstrand distance is defined as the mean of distances between the centers of mass of all peptides.

The order of alignment in the system, represented by the nematic order parameter, P_2, is calculated using WORDOM[37,38] and is defined as

$$P_2 = \frac{1}{N}\sum_{i=1}^{N}\frac{3}{2}(\hat{z}_i\cdot\hat{d})^2 - \frac{1}{2} \quad (1)$$

Here, N is the number of peptides, $\hat{z}_i$ is a vector connecting the second and second-to-last α-carbons of peptide i, and $\hat{d}$ is the director. The nematic order parameter can be employed to determine the overall order of alignment, as well as for the local positioning if only the alignment with a peptide's closest neighbor is considered. Values for the nematic order parameter range from $-\frac{1}{2}$, in the case of complete disorder, to a value of 1 for perfectly aligned peptides. In the case of a random distribution, $\overline{P}_2 = \sqrt{81/40\pi N}$ describes the expected P_2 value for a system with N peptides. To obtain information about transitions within a system, the weighted histogram analysis method (WHAM) is used to determine the system's average potential energy $U(T)$ as a function of temperature.[22,39] From this energy, the heat capacity at constant volume, $C_V = (\partial U/\partial T)_V$, is calculated.

The free energy as a function of order parameter was computed from $F = -k_B T \ln \mathcal{P}(\overline{c})$, where k_B is the Boltzmann constant, T the temperature, and $\mathcal{P}(\overline{c})$ the normalized probability of finding a system in a certain configuration with order parameter $\overline{c}$.

Forward Flux Sampling. The long time scales on which amyloid fibril formation occurs are related to high free energy barriers, making fibril nucleation a rare event. Enhanced sampling methods can address such rare events but require knowledge of the correct reaction coordinate which is often not available. The use of transition path sampling (TPS) alleviates this problem.[40−44] Within the path sampling framework, the transition interface sampling (TIS) and the forward flux sampling (FFS) methods can efficiently compute rate constants.[45,46] In TIS and FFS, the initial state A and final state B are separated in terms of an order parameter λ such that $\lambda < \lambda_A$ in region A and $\lambda > \lambda_B$ in region B. The boundaries of A and B are therefore defined by λ_A and λ_B (or λ_0 and λ_n, respectively). Between A and B, several interfaces $i = 1, ..., n-1$ are defined such that $\lambda_{i+1} > \lambda_i$. The expression for the rate constant k_{AB} is given by

$$k_{AB} = \frac{\overline{\Phi}_A}{\overline{h}_A}P(\lambda_B|\lambda_A) \quad (2)$$

where $\overline{\Phi}_A$ is the time-average of the effective positive flux of trajectories from A that cross λ_A and $\overline{h}_A$ is the average probability to be in A. The crossing probability $P(\lambda_B|\lambda_A)$ is the conditional probability that a trajectory from A reaches B before it returns to A, which can be expressed as a product

$$P(\lambda_B|\lambda_A) = \prod_i P(\lambda_{i+1}|\lambda_i) \quad (3)$$

where $P(\lambda_{i+1}|\lambda_i)$ denotes the conditional crossing probability that a trajectory from A that reaches i also reaches $i+1$, before returning to A. Here we employ the direct forward flux sampling (FFS) algorithm[47] to study the primary fibril nucleation of the hexapeptides. The direct FFS algorithm is initiated with a straightforward MD run in region A, during which the order parameter λ is followed over time.[47] Each time the trajectory crosses boundary λ_A in the positive direction, the configuration is stored until a total of N_f configurations are generated. This procedure forms a set of starting configurations on λ_A for trial runs toward the next interface (λ_1) and simultaneously provides an estimate of the flux $\overline{\Phi}_A = N_f/\tau$, where τ is the total length of the trial run. Next, the algorithm initiates several trial runs from a randomly selected starting configuration on interface i. If the trajectory reaches interface λ_{i+1}, the end-point is stored and the run is terminated. The trial run is also terminated if the order parameter returns to state A. Thus, each trajectory is free to recross previous interfaces before crossing the next. This procedure is repeated until C_{i+1} configurations are generated on interface $i+1$, and the number of runs needed to achieve this threshold is stored as M_i.

The FRESHS software package is used to carry out the forward flux sampling simulations, as it complies well with ESPResSo.[48] *PHF6** and *PHF6* were modeled using the peptideB force field. For all FFS simulations, $N = 12$ peptides were solvated in a box with edges of 102 Å, consistent with a concentration of ∼20 mM. Water was implicitly modeled using Langevin dynamics with a main time step of 1 fs and a friction coefficient of 1.0 ps^{-1}.

Results from coarse-grained REMD simulations show that *PHF6* self-assembles into two parallel β-sheets of six monomers; therefore, the order parameter is defined as the number of in-register C_α contacts in the two largest clusters. If no clusters are present, the maximum number of in-register C_α contacts between two single peptides is taken. Defining a proper distribution of order parameters is done on the basis of previous works on a similar subject,[22] and is fine-tuned by a set of trial simulations. After calibration, five separate forward ($A \rightarrow B$) and five separate reversed simulations ($B \rightarrow A$) were performed using the settings shown in Table 1, and paused every 1 ps to calculate the order parameter. Here i is the interface number, C_i is the amount of paths collected up to that point, and λ_i is the corresponding order parameter. To carry out the reversed FFS simulation, we define the auxiliary order parameter λ_i' as $\lambda' = \lambda_A + \lambda_B - \lambda$.

Table 1. Definition of Interfaces for FFS Simulations of the *PHF6* and *PHF6 Systems[a]**

	PHF6			*PHF6**		
i	C_i	λ_i	λ_i'	C_i	λ_i	λ_i'
0	200	8 (A)	8 (B)	30	4 (A)	4 (B)
1	175	12	12	29	8	8
2	155	16	16	28	12	12
3	140	20	20	27	16	16
4	130	24	24	26	20	20
5	123	28	28	25	24	24
6	114	32	32	24	28	28
7	110	36	36	23	32	32
8	108	40	40	22	36	36
9	105	44	44	21	40	40
10	102	48	48	20	44	44
11	100	52 (B)	52 (A)	19	48 (B)	48 (A)

[a] C_i is the number of target pathways. λ_i denotes the ith interface value for the forward FFS run, λ_i' for the reverse.

DOI: 10.1021/acs.jpcb.6b07045
J. Phys. Chem. B 2017, 121, 3250−3261

The simulations were carried out at a temperature of $T/(300\ \mathrm{K}) = 1.138$ (~340 K), which is slightly below the ordering transition temperature, T_0. The value of T_0 could not be obtained for *PHF6**, however, and a similar T_0 to that of *PHF6* was used, namely, $T/(300\ \mathrm{K}) = 1.12$ (~336 K).

The analysis of all FFS simulations was carried out using home-written scripts. If an FFS simulation is realized in both directions, i.e., $A \rightarrow B$ and $B \rightarrow A$, the free energy, $F(N_{C_\alpha})$, for a certain order parameter N_{C_α}, can be extracted from the averaged simulation data as

$$F(N_{C_\alpha}) = -k_B T \ln \rho(N_{C_\alpha}) \tag{4}$$

where $\rho(N_{C_\alpha})$ is the probability to observe the number of in-register C_α atoms, and is given by[49]

$$\rho(N_{C_\alpha}) = \rho_A \Phi_{A,0} \tau_+(N_{C_\alpha}; \lambda_A) + \rho_B \Phi_{B,n} \tau_-(N_{C_\alpha}; \lambda_B) \tag{5}$$

Here ρ_A and ρ_B are the steady state probabilities of being in A and B, respectively, and are related via the detailed balance relation $\rho_A k_{AB} = \rho_B k_{BA}$. The flux out of either state $\Phi_{A,0}$ and $\Phi_{B,0}$ to the first interface is calculated during the initial straightforward MD simulation in the stable states. The function $\tau_{+,-}(N_{C_\alpha}; \lambda_A)$ denotes the average time a system coming from either A or B has spent at a certain order parameter (N_{C_α}) and is, for the forward simulation, computed as[49]

$$\tau_+(N_{C_\alpha}; \lambda_A) = \pi_+(N_{C_\alpha}; \lambda_A) + \sum_{i=1}^{n-1} \pi_+(N_{C_\alpha}; \lambda_i) \prod_{j=0}^{i-1} P(\lambda_{j+1}|\lambda_j) \tag{6}$$

where $\pi_+(N_{C_\alpha}; \lambda_i)$ is the average time a run originating from interface λ_i spent at order parameter N_{C_α}. The function $\tau_-(N_{C_\alpha}; \lambda_B)$ is calculated in a similar fashion with data from the reverse simulations.

To study the nucleation pathway, a cluster analysis is performed by evaluating the reactive pathways, i.e., all paths that reached interface B.[36] For every snapshot, all clusters are classified, after which they are compared with the previous snapshot. The number of grown, shrunken, and unchanged clusters of size n are registered in histograms $h_{\mathrm{grow}}(n)$, $h_{\mathrm{shrink}}(n)$, and $h_{\mathrm{same}}(n)$, respectively. This process is repeated until every frame is compared with the one preceding it. The probability $P_x(n)$ of a cluster of size n to belong to a certain category $x \in$ {grow, shrink, (remain the) same}, $P_x(n)$, is

$$P_x(n) = \frac{h_x(n)}{h_{\mathrm{grow}}(n) + h_{\mathrm{shrink}}(n) + h_{\mathrm{same}}(n)} \tag{7}$$

Sometimes it can be useful to compare only two of the three probabilities against each other. In that case, the value of the third histogram can be left out of the denominator.

RESULTS

PHF6* **and *PHF6* Dimerization.** We performed REMD simulations of dimer systems of *PHF6** and *PHF6*. The replica flow of both hexapeptides (see Figure 2) exhibits a good diffusivity of replicas through temperature space. The free energy landscapes as a function of the average interstrand distance for the two hexapeptides in Figure 3A and D show a nearly identical landscape for both *PHF6** and *PHF6*. The free energy minimum at around 4 Å implies that the monomers are more likely to be in close proximity and form a dimer.

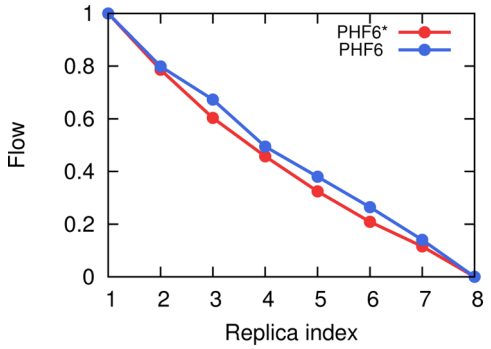

Figure 2. Replica flow of the coarse-grained dimer simulations.

The free energy landscape of the nematic order parameter P_2, indicating the degree of alignment of the monomers in Figure 3B and E, is similar for both *PHF6** and *PHF6*. The clear minimum at a relatively high nematic order parameter P_2 implies a proper alignment. Furthermore, Figure 3C and F shows that all six of the C_α atoms are in-register with their counterpart, which coincides with an alignment in a parallel fashion.

PHF6* **and *PHF6* Aggregation.** Next, we performed REMD simulations of the multiple peptide systems $N = 8$, $N = 12$, and $N = 20$. The replica flow for every system is shown in Figure 4. The *PHF6** system shows an excellent replica flow for $N = 8$ and $N = 12$. Even though $N = 20$ deviates slightly from linear behavior, it shows a reasonably good replica flow, indicating sufficient diffusivity of replicas through temperature space. A different situation occurs for *PHF6*, where $N = 12$ and $N = 20$ show a sigmoid-like curve. This indicates a much smaller although nonzero replica exchange ratio caused by a large difference in potential energy between systems on either side of the phase boundary. The $N = 8$ system, being a smaller system, still exhibits a reasonable flow.

The aggregation transition can be viewed as a (finite size) phase transition, and hence should have thermodynamic signatures such as a peak in the heat capacity. Figure 5 shows the calculated heat capacity for *PHF6** and *PHF6* with $N \in \{8, 12, 20\}$ peptides. *PHF6** shows a peak at temperatures around 450 K, which corresponds to the peptide condensation peak, describing the transition from the gas (dilute phase) to the liquid (disordered oligomer phase). Other than that, no significant peaks are found for $N = 8$ and $N = 12$ peptides and only a small rise in C_V can be observed around 300 K for $N = 20$, which might be an indication of a transition. Nevertheless, visual inspection of the configuration shows no strong sign of order. In contrast, for the *PHF6* system, very distinct peaks occur for $N = 8$, 12, and 20 peptides, akin to a phase transition. This peak occurs in a temperature range of 330 ± 20 K and corresponds to the transition between a disordered liquid at high temperatures and a systematic fibril-like oligomer arrangement at lower temperatures. For $N = 12$, the corresponding transition temperature T_0 is $T/(300\ \mathrm{K}) = 1.143$ (~343 K). The change in transition temperature for different numbers of peptides is probably caused by the system size and/or poor replica flow.

Focusing on the $N = 12$ peptides, using a cluster and order parameter analysis, we compute the fraction of peptides that belong to an aligned (β-sheet) cluster. Upon an ordering

DOI: 10.1021/acs.jpcb.6b07045
J. Phys. Chem. B 2017, 121, 3250−3261

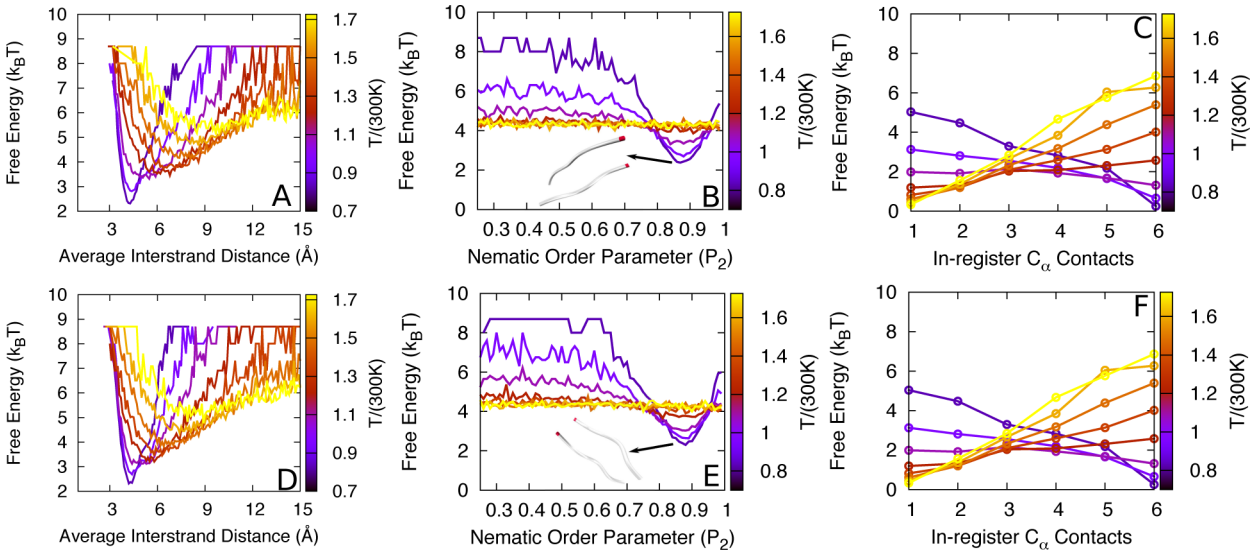

Figure 3. Free energy landscapes for *PHF6** dimer and *PHF6* dimer as a function of several order parameters at different temperatures. Left (A, D): average interstrand distance. Middle (B, E): the relative orientation of the monomers. Right (C, F): number of in-register Ca contacts.

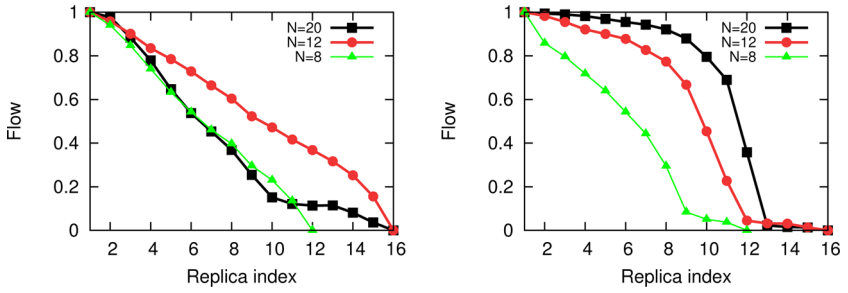

Figure 4. Replica flow of the coarse-grained simulations for *PHF6** (left) and *PHF6* (right).

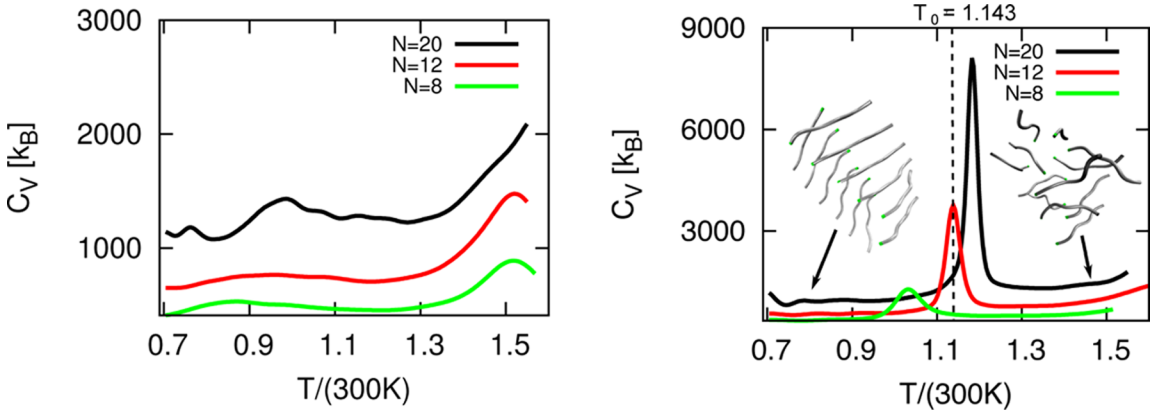

Figure 5. Heat capacity, C_V, for the *PHF6** (left) and *PHF6* (right) simulations.

transition, the aggregation fraction as a function of temperature exhibits an inflection point. In Figure 6, the *PHF6** system shows an increasing aggregation fraction at lower temperatures, up to a value around 0.5 but not higher, as it fails to form an ordered fibril.[22] This is in agreement with Figure 5 (left), in which also no transition is observed. In contrast, for the *PHF6* system, the aggregation fraction as a function of temperature increases from zero for a disordered system at high temperatures to unity, indicating a fully ordered system at low temperature. The inflection point in the sigmoidal curve represents the transition temperature T_0 and is found at the same value that is suggested in Figure 5.

The free energy landscapes as a function of the total number of in-register C_α contacts for *PHF6** and *PHF6* are shown in Figure 7. In the case of *PHF6**, a decrease in temperature goes hand in hand with a shift of the free energy minimum toward higher values of in-register contacts, which indicates a higher degree of organization at lower temperatures. The minimum observed at 210 K lies close to $N_{C_\alpha} = 35$, which is approximately half the theoretical maximum of $(11 \times 6 =)$ 66. This behavior is known for substances which polymerize at lower temperature and form so-called cluster liquids.[22] In such liquids, small clusters are observed but no fibrils are formed.

DOI: 10.1021/acs.jpcb.6b07045
J. Phys. Chem. B 2017, 121, 3250−3261

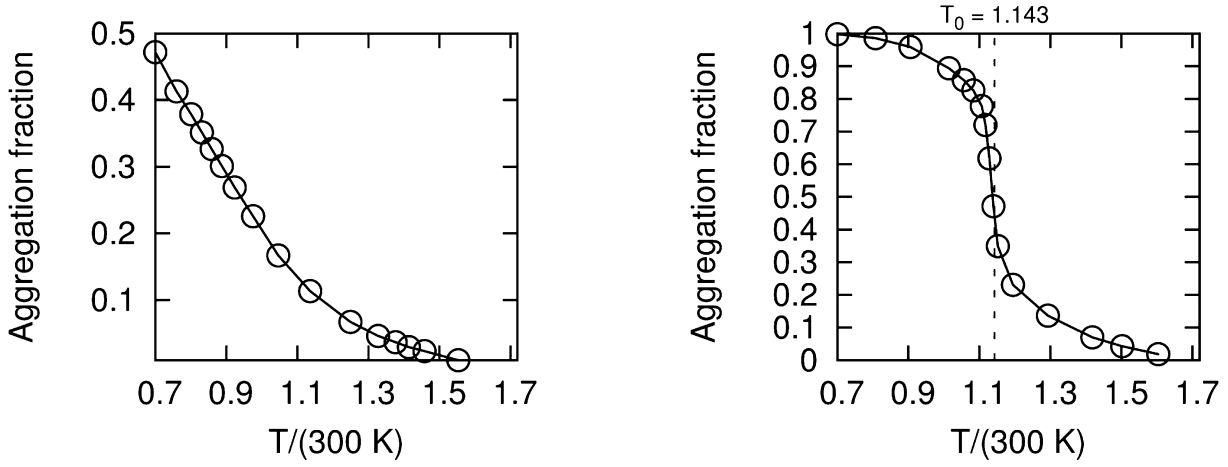

Figure 6. Fraction of aggregated peptides plotted over the temperatures for N = 12 peptides of *PHF6** (left) and *PHF6* (right), with the corresponding transition temperature T_0.

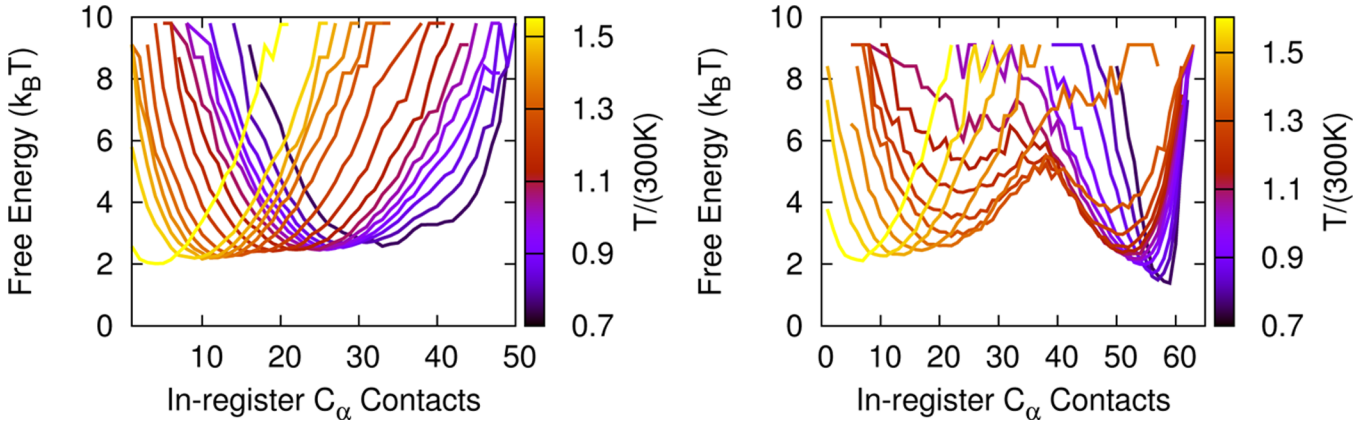

Figure 7. Free energy vs the number of in-register C_α contacts for N = 12 peptides of *PHF6** (left) and *PHF6* (right).

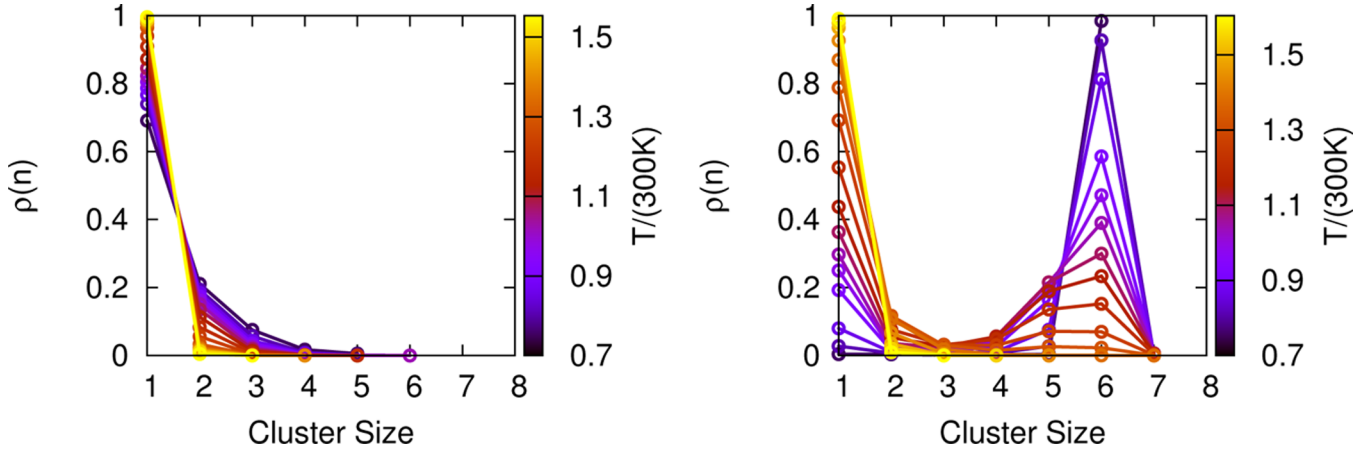

Figure 8. Cluster size distribution for N = 12 peptides of *PHF6** (left) and *PHF6* (right).

Even though *PHF6* does not reach the theoretical maximum of 66 in-register contacts either, it shows a significantly different behavior than *PHF6**. A free energy minimum at values as high as 60 in-register contacts at a temperature $T/(300\ \mathrm{K}) = 0.7$ (~210 K) suggests a degree of order consistent with full fibrilization.

Figure 8 shows the normalized cluster size distributions $\rho(n)$. In the case of *PHF6**, the exponential decrease in probability for increasing cluster sizes indicates that no fibrilization takes place. At low temperature (purple line), dimers, trimers, and tetramers are present, indicating the existence of a polymerized or cluster liquid.[22]

In the case of *PHF6*, the clear peak at n = 6 monomers indicates that this peptide forms stable aggregates and suggests that fibrils consist of two sheets of six peptides. We found no evidence for the formation of different combinations of sheets, such as a single β-sheet consisting of 12 monomers, or a pentamer/heptamer sheet combination, an octamer/tetramer

DOI: 10.1021/acs.jpcb.6b07045
J. Phys. Chem. B 2017, 121, 3250−3261

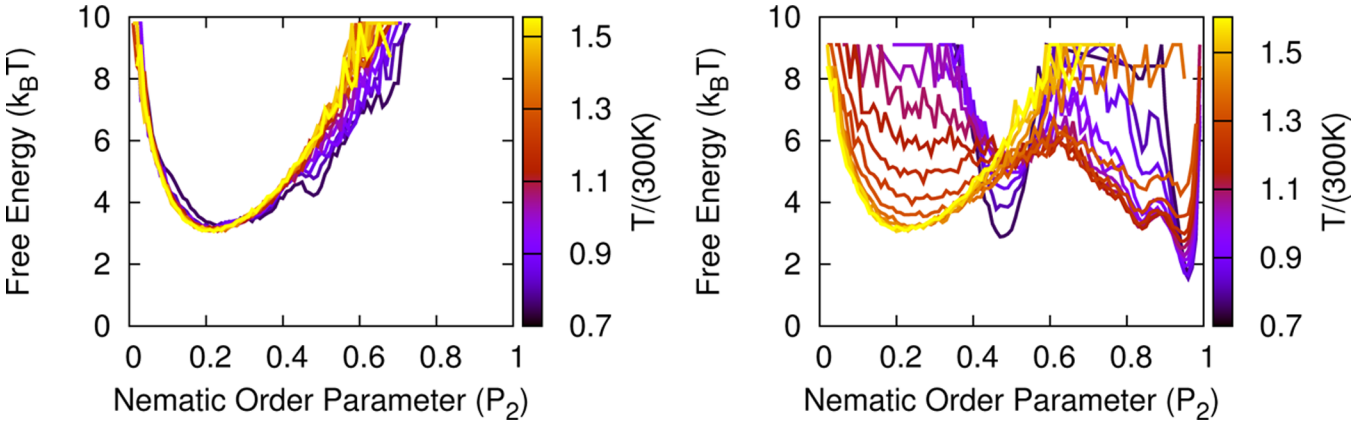

Figure 9. Free energy vs the nematic order parameter P_2 for $N = 12$ peptides of *PHF6** (left) and *PHF6* (right).

sheet combination, or even the combination of three tetramer sheets.

Figure 9 shows the free energy landscape as a function of the overall degree of alignment of the system using the nematic order parameter P_2. The free energy minima of *PHF6** remain the same for all temperatures, which coincides with the expected value for a randomly ordered system where $N = 12$, as $\overline{P}_2 = \sqrt{81/40\pi 12} \approx 0.23$, confirming again *PHF6**'s incapacity to form fibrils. Figure 9 (right) shows a similar free energy curve at the same location for *PHF6* at high temperatures where the oligomer is disordered. At lower temperatures, two free energy minima are observed. The minimum at $P_2 \approx 0.5$ corresponds to a state in which the monomers of the first sheet are not perfectly aligned with the monomers of the second sheet, whereas the second minimum, at 0.95, belongs to a configuration where all monomers are well-aligned. Visual inspection of the simulations shows a parallel alignment of the monomers in each sheet, whereas the sheets are oriented in opposing directions.

Primary Nucleation Kinetics of *PHF6*. We performed FFS simulations at a temperature of $T/(300\ \mathrm{K}) = 1.138$ (~340) K for the *PHF6* systems, starting at an initial disordered liquid state A and ending at the final fibril configuration B. Table 2 shows an overview of the resulting crossing probabilities between each set of neighboring interfaces along with the average path length, $\overline{l}$, for the FFS simulation of *PHF6*. The crossing probability is relatively constant (around 0.2) up to λ_6, corresponding to 32 in-register contacts, indicating a steep barrier. At higher values, the crossing probability steadily increases as a function of λ, indicating that the barrier becomes less steep.

Table 2. Crossing Probabilities, Flux (Φ), and Rate Constant (k) for the FFS Simulation of *PHF6*

i	$P(\lambda_{i+1}\|\lambda_i)$	$\overline{l}_{\mathrm{forward}}$ (ps)	$P(\lambda'_{i+1}\|\lambda'_i)$	$\overline{l}_{\mathrm{backward}}$ (ps)
1	0.1871	5	0.2406	4
2	0.1852	6	0.2045	3
3	0.1846	15	0.2996	8
4	0.1999	52	0.2957	19
5	0.2017	73	0.2604	49
6	0.2562	153	0.3105	81
7	0.4178	207	0.2700	204
8	0.6024	399	0.2467	446
9	0.6680	886	0.3724	476
10	0.8326	1222	0.3940	784
B	0.9188	1645	0.3803	1344
Φ	$5.5 \times 10^{10}\ \mathrm{s}^{-1}$		$6.2 \times 10^{10}\ \mathrm{s}^{-1}$	
k	$6.7 \times 10^{5}\ \mathrm{s}^{-1}$		$5.9 \times 10^{4}\ \mathrm{s}^{-1}$	

The reversed simulation ($B \rightarrow A$, dissolution of the fibril) shows a relatively constant crossing probability of 30 ± 10%. The qualitative difference in crossing probability behavior between forward and reverse FFS simulations suggests some degree of hysteresis; i.e., the association and dissociation processes follow different pathways.

The flux, Φ, and rate constants, k, are also reported in Table 2. Clearly, self-assembly of *PHF6* fibrils proceeds faster than its dissociation, with the forward reaction rate $k_{AB} = 6.7 \times 10^5\ \mathrm{s}^{-1}$ more than 10 times higher than the reverse reaction rate $k_{BA} = 5.9 \times 10^4\ \mathrm{s}^{-1}$. The equilibrium constant is $K = \frac{k_{AB}}{k_{BA}} = 10.29$ corresponding to a difference in free energy between the two states, $\Delta F = -k_B T \ln K = -2.43\ k_B T$. This negative value of ΔF confirms the system's tendency to form fibrils at this temperature. The corresponding equilibrium (steady state) population, $\rho_B = \frac{k_{BA}}{k_{AB} + k_{BA}} = 0.919$, indicates the probability of finding the system in state B, which is much larger than the probability of finding the system in state A, namely, 0.081 as $\rho_A + \rho_B \approx 1$ at this temperature.

Figure 10 shows the (partial) free energy landscape for the forward $A \rightarrow B$ as well as the reversed $B \rightarrow A$ simulation. The free energy curves fluctuate near the borders due to poor sampling of the fully dissociated and associated state during the forward and backward simulations, respectively.

Combining the forward and backward free energies and weighting them properly by applying eq 4 results in the overall free energy landscape as a function of the number of in-register contacts, which is also depicted in Figure 10. Apart from several small metastable minima, one distinct free energy barrier is observed near 30 in-register contacts. This value is roughly in agreement with the point where the forward crossing probabilities start to increase. The middle inset of Figure 10 (right) shows a transition structure from the forward paths, consisting of several half formed β-sheets. This structure is just one of the possible transition states that can be seen as critical nuclei in the primary nucleation process of fibril formation. Such structures have relatively high free energy as the peptides have lost configurational entropy but have not yet gained sufficient stabilization from favorable interactions, such as the

DOI: 10.1021/acs.jpcb.6b07045
J. Phys. Chem. B 2017, 121, 3250−3261

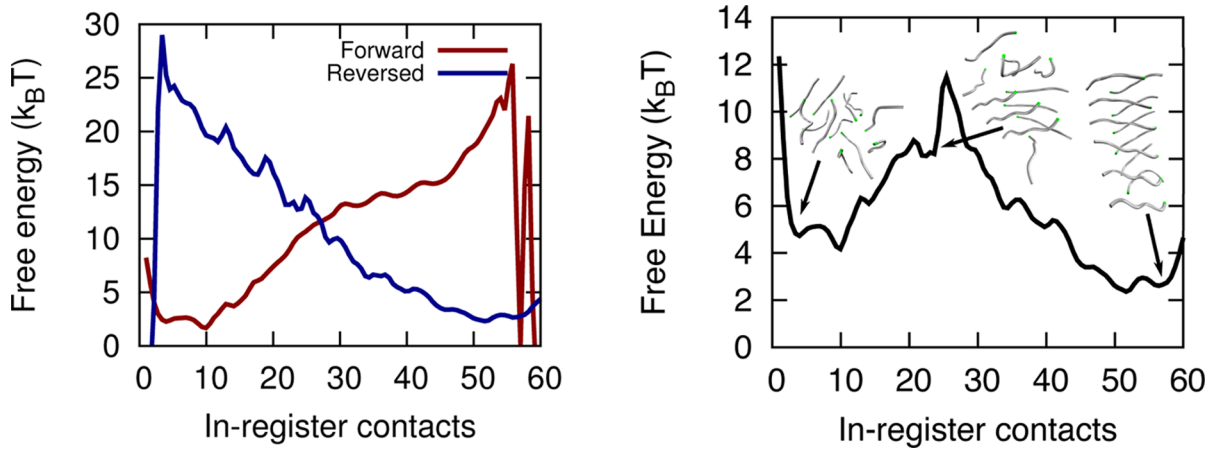

Figure 10. Free energy landscapes for the number of in-register C_α contacts for *PHF6*. (left) Contributions of the forward and backward FFS runs to the free energy. (right) Combined free energy. Several typical structural snapshots are indicated.

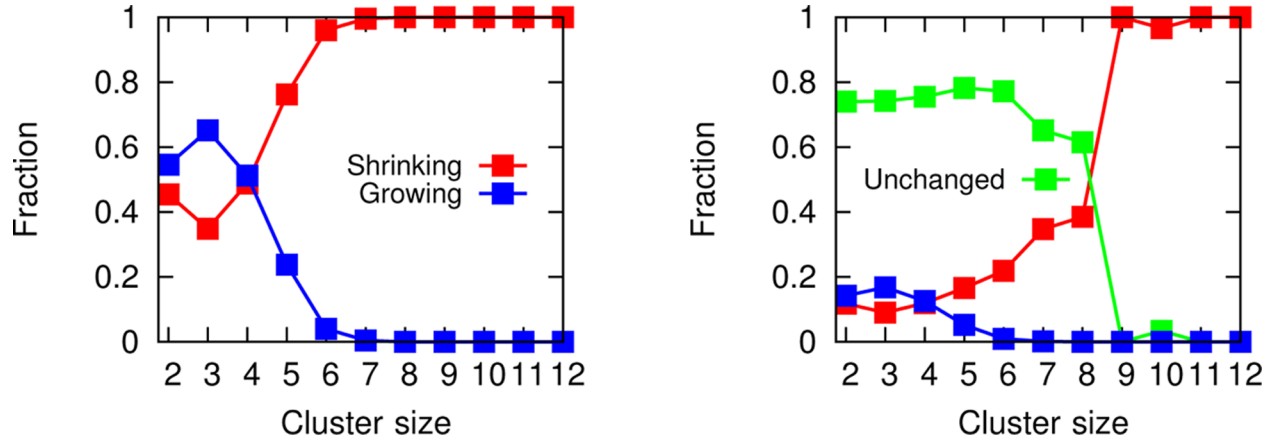

Figure 11. (left) Cluster growth and shrinking probability as a function of cluster size along the TPE. (right) Cluster growth, shrinking, and stability probability as a function of cluster size.

formation of the second sheet. The free energy difference between state *A* and state *B* of ∼2 k_BT approximates the calculated free energy difference of 2.43 k_BT. This result is in agreement with the REMD predictions in Figure 7(right).

The transition path ensemble (TPE) of the fibril formation is available from the FFS simulation. We analyze these paths to obtain insight into the growth kinetics of fibril-like structures in the oligomer. The kinetic behavior of the peptide clusters in the oligomer along the TPE is shown in Figure 11, which compares the growth probability, P_{grow}, with the shrink probability, P_{shrink}, such that the sum adds up to unity. Clusters consisting of up to four monomers have the tendency to grow, whereas larger clusters are more likely to reduce in size. This lack of growth is most likely due to depletion of monomers in the droplet. In addition, it appears to be more favorable for a monomer to dimerize and start forming a second sheet than to anchor to an existing cluster of four. Figure 11 (right) includes the probability that a cluster remains of the same size, which *de facto* is a measure of an oligomer's stability. The probability P_{same} increases up until $n = 6$, after which the stability declines. This behavior agrees with the observation that two sheets of six peptides are formed in the coarse-grained REMD simulations. Clusters containing more than eight monomers seem to shrink at all times, implying instability.

We also performed an FFS simulation of *PHF6**. The crossing probabilities are reported in Table 3 and are remarkably low, and become basically zero at λ_9, corresponding to 40 in-register contacts. The relatively short transition pathways at higher λ's (∼10% of the path length observed for *PHF6*) indicate that the encountered states are coincidental structures and do not correspond to a viable transition path. The computed rate for this process is lower than 10^{-10} s^{-1}, corresponding to once per every few centuries. These

Table 3. Crossing Probability for the FFS Simulation of *PHF6 along with the Average Path Length ($\bar{l}$)**

i	$P(\lambda_{i+1}\|\lambda_i)$	$\bar{l}_{forward}$ (ps)	$P(\lambda'_{i+1}\|\lambda'_i)$	$\bar{l}_{backward}$ (ps)
1	0.5912	6	0.4801	2
2	0.0111	4	0.3742	3
3	0.0126	6	0.5513	7
4	0.0022	11	0.6042	13
5	0.0094	12	0.6653	35
6	0.0016	64	0.7871	69
7	0.0239	22	0.7675	137
8	0.0033	39	0.7341	180
9	5.2912×10^{-5}	187	0.9338	191
10	n/a	n/a	0.9348	223
11	n/a	n/a	0.9524	250
Φ	1.36×10^{10} s^{-1}		7.0×10^{10} s^{-1}	
k	1.55×10^{-10} s^{-1}		8.4×10^{8} s^{-1}	

DOI: 10.1021/acs.jpcb.6b07045
J. Phys. Chem. B 2017, 121, 3250−3261

observations support the hypothesis that *PHF6** is unable to form stable β-sheet-based fibrillar aggregates. To test this hypothesis further, we initiated a reverse FFS simulation, starting from a fibril structure taken from the *PHF6* FFS simulations. The reverse FFS simulations showed that this structure was not stable, and fell apart very quickly. Indeed, the dissociation rate in Table 3 is 4 orders of magnitude higher than that of *PHF6*, and at least 17 orders of magnitude faster than the nucleation rate of *PHF6**.

DISCUSSION

While the dimer properties of *PHF6* and *PHF6** are almost identical, when looking at the tendency of *PHF6** and *PHF6* to self-assemble into fibril-like structures, a remarkable difference is encountered. The simulations show that *PHF6** is not able to form stable aggregates, which unfortunately cannot be straightforwardly compared to the literature, as no crystal structure has yet been reported for this peptide.[50] In contrast, *PHF6* appears to be very well able to form fibrils. Our results can be compared to the study by Li et al.,[25] who performed Monte Carlo simulations of the *PHF6* fragment employing an implicit solvent all-atom model. They found evidence for a nucleation process, similar to our results. However, as their simulation was done at lower temperature, the authors report a very fast aggregation and observed hardly any nucleation barrier. For a system of 12 peptides, they observed the formation of stable oligomers consisting of two sheets held together by hydrophobic interactions. In contrast to our findings, initially these sheets contain a mixture of parallel and anti parallel strands, which have to reorder in order to initiate further fibril growth.

The higher aggregation propensity of *PHF6* with respect to *PHF6** is in accordance with numerous studies.[13,18,19,21,51,52] The difference can be accounted for by looking at the difference in amino acid sequence and in their corresponding interaction coefficients, Table 4. Here ϵ_i' is an averaged parameter determining the strength of interaction between specific residues. The main difference between the two peptides lies in the hydrophobic triad, VIX, where X is asparagine for *PHF6** and tyrosine for *PHF6*. Asparagine has a significantly lower interaction coefficient than tyrosine, resulting in an ~40% lower interaction with the other residues, which apparently can make the difference between aggregating or not.

Experiments show that eliminating *PHF6** from *R2/wt* does still lead to some tau aggregation, while removing *PHF6* prevents all aggregation.[19] However, *PHF6**, which is part of *R2/wt*, does not fibrilize, whereas *PHF6* does form fibrils. This observation is rather counterintuitive and seems to contradict the observation that *R2/wt* is more aggregation prone than *R3/wt*.

The disability of *PHF6**'s to form a stable fibril under the peptideB force field is confirmed by the results obtained from the FFS simulations. As mentioned before, we are unable to compare this to experiments, as no crystal structure has been reported for this peptide.[50] However, the fact that our simulations seem to predict that this hexapeptide is not able to form fibrils might explain this lack of crystal structure.

The *PHF6* $N = 12$ system forms fibril nuclei consisting of two β-sheets of six peptides in case. In these sheets, monomers are stacked in a parallel fashion, whereas the two sheets lie in an antiparallel fashion. This structure has also been experimentally observed for this hexapeptide and is described as class 1 in the eight classes of steric zippers, which describes the fibril organization of aggregation prone peptides.[50,53,54]

On the basis of visual inspection and cluster analysis, we can propose a nucleation mechanism, as visualized in Figure 12. Starting from a liquid of unorganized monomers (i), a single β-sheet is formed consisting on average of four monomers (ii). Even though occasionally more peptides lock onto the tetramer and enlarge the existing sheet (iii), the most likely next step in the process involves the formation of a second β-sheet (iv). Note that in most cases the two sheets form almost simultaneously or very rapidly succeeding each other. The next step is the alignment of the two existing sheets (v). The overall barrier seems to have been reached in the last step, where the remaining peptides anchor to the existing oligomer and form a fibril-like structure (vi).

While the reverse process in principle should follow the same mechanism due to the detailed balance, a certain amount of

Table 4. Each Residue with Corresponding ϵ_i'

ϵ_i' (*PHF6**)	5.43	1.74	6.79	6.79	1.54	0.99
residue	V	Q	I	$\frac{I}{V}$	$\frac{N}{Y}$	K
ϵ_i' (*PHF6*)	5.43	1.74	6.79	5.43	4.29	0.99

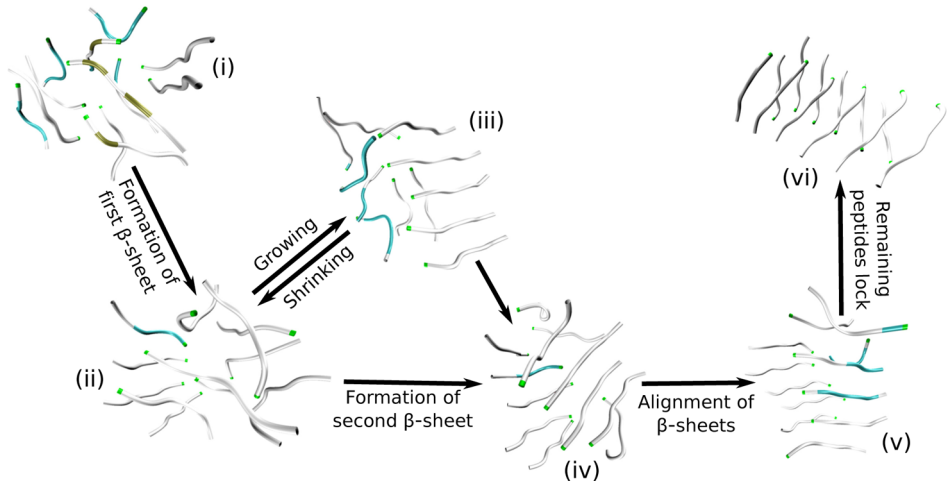

Figure 12. Schematic representation of the *PHF6* nucleation mechanism inferred from the forward FFS paths.

DOI: 10.1021/acs.jpcb.6b07045
J. Phys. Chem. B 2017, 121, 3250−3261

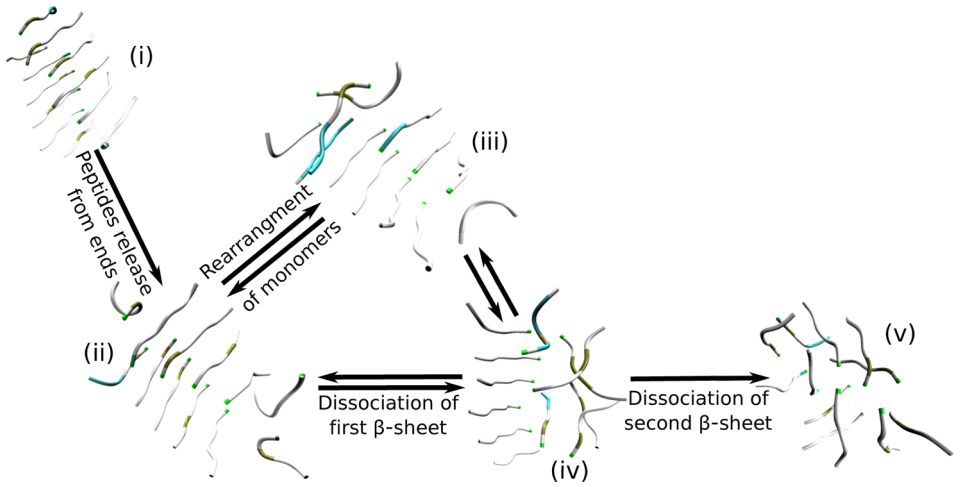

Figure 13. Schematic representation of the *PHF6* dissociation mechanism inferred from the reverse FFS paths.

hysteresis can be expected. We therefore also inspected the dissociation process in the reverse FFS path ensemble (for a visual representation, see Figure 13). In the dissociation process, the peptides of the formed fibril (i) first melt at the ends of the fibril (ii) and rearrange (iii). Then, one of the β-sheets melts first (iv), after which the second one melts (v). There are many similarities with the nucleation pathways, such as the presence of the 1-β-sheet intermediate state, but there are also striking differences. For instance, the locking transition of the two β-sheets observed in the nucleation process does not occur during melting. Notwithstanding these differences, the reverse mechanism is in agreement with the nucleation pathways, showing that the FFS sampled more or less the correct path ensemble.

These simulations confirm that this peptide nucleates via a two-step nucleation (2SN), where the first step is the appearance of nonfibrillar disordered oligomers in the solution after which they convert into fibrils, in agreement with Ostwald's step rule. Indeed, 2SN has been known to occur for peptides with a strong hydrophobic nature.[22,36,55]

The barrier of 8 k_BT predicted by the FFS simulations in Figure 10 seems in reasonable agreement with the fibrilization rate of 6.70×10^5 s^{-1}, assuming a transition state theory prefactor on the order of 10^9 s^{-1}. Any underestimation of the barrier is probably caused by plotting the free energy as a function of an approximate order parameter, and the presence of multiple pathways. In fact, the predicted rate of 6.70×10^5 s^{-1} on itself is a very high rate for a process that in the central nervous system occurs on a time scale of months to years. This overestimation of rate can be attributed to several reasons. First, molecular dynamics in the CG force field are faster compared to all-atom force fields with an explicit solvent, due to their softer effective potentials and the use of an implicit solvent. Second, the simulations are done at a relatively high concentration. Indeed, at such high concentrations, even straightforward MD already shows some spontaneous aggregation within a few hundred nanoseconds.[24] The concentration of intracellular *tau* lies around 3 μM, the majority of which (>99%) is tightly bound to the microtubule.[56,57] Even though the free *tau* concentration is elevated in patients with Alzheimer's disease or other forms of dementia, the concentrations used for this study are much higher than those in the human brain.[58−60] Moreover, no other molecules were included that might interfere or slow down the assembly of *PHF6* in the brain.

CONCLUSIONS

Experimental work has shown that *PHF6** and *PHF6* are important sequences for *tau* to aggregate.[19] In our simulations, we observe that *PHF6** and *PHF6* dimerize, as do the *R2/wt* and *R3/wt* sequences. On the other hand, while both hexapeptides aggregate into a disordered oligomer, only the *PHF6* undergoes a two-step nucleation and converts into a fibrillar structure consisting of two parallel β-sheets. The *PHF6** peptide systems do not show any sign of fibril formation in our REMD simulations but remain in a disordered polymerized liquid state. It follows that, while *PHF6** could assist in the aggregation of *tau*, the hexapeptide itself is not interacting strongly enough to induce fibrilization.

The kinetics of *PHF6** and *PHF6* conversion from a disordered liquid oligomer into a fibril-like structure was investigated using forward flux sampling simulations. The *PHF6* peptide forms fibrils with a rate constant of $k_{AB} = 6.70 \times 10^5$ s^{-1} at a temperature of 340 K, whereas the *PHF6** did not fibrilize at all. Reverse FFS simulations confirmed that a *PHF6** fibril is unstable and quickly falls apart.

The results in this work give qualitative insight into the primary nucleation kinetics of short fragments of the tau protein. The stability and kinetic predictions should be taken qualitatively, as the force fields are approximate. Moreover, the use of a CG force field will render the predicted kinetics too fast, due to smoothing of the potentials. Nevertheless, our results seem to indicate a physical reason for the fact that a *PHF6** steric zipper crystal structure is not available. These results are also in agreement with the experimental observation that, while *PHF6* is a prerequisite sequence for tau aggregation, *PHF6** merely enhances aggregation.[19]

In future work, we will investigate the fibrilization of *R2/wt* and *R3/wt* with the CG models. In addition, we will improve the predictions of this work by using full atomistic models to access the kinetics of the hexapeptides.

AUTHOR INFORMATION

Corresponding Author

*E-mail: p.g.bolhuis@uva.nl.

DOI: 10.1021/acs.jpcb.6b07045
J. Phys. Chem. B 2017, 121, 3250−3261

Notes

The authors declare no competing financial interest.

REFERENCES

(1) Jeganathan, S.; von Bergen, M.; Mandelkow, E.-M.; Mandelkow, E. The Natively Unfolded Character of Tau and Its Aggregation to Alzheimer-like Paired Helical Filaments. *Biochemistry* **2008**, *47*, 10526−10539.

(2) Kolarova, M.; Garcia-Sierra, F.; Bartos, A.; Ricny, J.; Ripova, D. Structure and Pathology of Tau Protein in Alzheimer Disease. *Int. J. Alzheimer's Dis.* **2012**, *2012*, e731526.

(3) Nogales, E. Structural Insights into Microtubule Function. *Annu. Rev. Biochem.* **2000**, *69*, 277−302.

(4) Hyams, J. S.; Lloyd, C. W. *Microtubules*; Wiley-Liss: New York, 1994.

(5) Weingarten, M. D.; Lockwood, A. H.; Hwo, S. Y.; Kirschner, M. W. A Protein Factor Essential for Microtubule Assembly. *Proc. Natl. Acad. Sci. U. S. A.* **1975**, *72*, 1858−1862.

(6) Cleveland, D. W.; Hwo, S.-Y.; Kirschner, M. W. Purification of Tau, a Microtubule-Associated Protein that Induces Assembly of Microtubules from Purified Tubulin. *J. Mol. Biol.* **1977**, *116*, 207−225.

(7) Gustke, N.; Trinczek, B.; Biernat, J.; Mandelkow, E.-M.; Mandelkow, E. Domains of tau Protein and Interactions with Microtubules. *Biochemistry* **1994**, *33*, 9511−9522.

(8) Breuzard, G.; Hubert, P.; Nouar, R.; Bessa, T. D.; Devred, F.; Barbier, P.; Sturgis, J. N.; Peyrot, V. Molecular mechanisms of Tau binding to microtubules and its role in microtubule dynamics in live cells. *J. Cell Sci.* **2013**, *126*, 2810−2819.

(9) Kanai, Y.; Chen, J.; Hirokawa, N. Microtubule Bundling by Tau Proteins In Vivo: Analysis of Functional Domains. *EMBO J.* **1992**, *11*, 3953−3961.

(10) Avila, J.; Lucas, J.; Perez, M.; Hernandez, F. Role of Tau Protein in Both Physiological and Pathological Conditions. *Physiol. Rev.* **2004**, *84*, 361−384.

(11) Hanger, D. P.; Anderton, B. H.; Noble, W. Tau Phosphorylation: the Therapeutic Challenge for Neurodegenerative Disease. *Trends Mol. Med.* **2009**, *15*, 112−119.

(12) Stoothoff, W.; Johnson, G. Tau Phosphorylation: Physiological and Pathological Consequences. *Biochim. Biophys. Acta, Mol. Basis Dis.* **2005**, *1739*, 280−297.

(13) Daebel, V.; Chinnathambi, S.; Biernat, J.; Schwalbe, M.; Habenstein, B.; Loquet, A.; Akoury, E.; Tepper, K.; Muller, H.; Baldus, M.; et al. β-Sheet Core of Tau Paired Helical Filaments Revealed by Solid-State NMR. *J. Am. Chem. Soc.* **2012**, *134*, 13982−13989.

(14) Cowan, C. M.; Mudher, A. Are Tau Aggregates Toxic or Protective in Tauopathies? *Front. Neurol.* **2013**, *4*, 114.

(15) Crowther, R. A.; Wischik, C. M. Image Reconstruction of the Alzheimer Paired Helical Filament. *EMBO J.* **1985**, *4*, 3661−3665.

(16) Ittner, L. M.; Götz, J. Amyloid-β and Tau; a Toxic Pas De Deux in Alzheimer's Disease. *Nat. Rev. Neurosci.* **2011**, *12*, 67−72.

(17) Nisbet, R. M.; Polanco, J.-C.; Ittner, L. M.; Götz, J. Tau Aggregation and Its Interplay with Amyloid-β. *Acta Neuropathol.* **2015**, *129*, 207−220.

(18) Sahara, N.; Maeda, S.; Murayama, M.; Suzuki, T.; Dohmae, N.; Yen, S.-H.; Takashima, A. Assembly of Two Distinct Dimers and Higher-Order Oligomers from Full-Length Tau. *Eur. J. Neurosci.* **2007**, *25*, 3020−3029.

(19) Li, W.; Lee, V. M.-Y. Characterization of Two VQIXXK Motifs for Tau Fibrillization in Vitro. *Biochemistry* **2006**, *45*, 15692−15701.

(20) von Bergen, M.; Barghorn, S.; Li, L.; Marx, A.; Biernat, J.; Mandelkow, E.-M.; Mandelkow, E. Mutations of Tau Protein in Frontotemporal Dementia Promote Aggregation of Paired Helical Filaments by Enhancing Local β-Structure. *J. Biol. Chem.* **2001**, *276*, 48165−48174.

(21) Ganguly, P.; Do, T. D.; Larini, L.; LaPointe, N. E.; Sercel, A. J.; Shade, M. F.; Feinstein, S. C.; Bowers, M. T.; Shea, J.-E. Tau Assembly: The Dominant Role of PHF6 (VQIVYK) in Microtubule Binding Region Repeat R3. *J. Phys. Chem. B* **2015**, *119*, 4582−4593.

(22) Luiken, J. A.; Bolhuis, P. G. Prediction of a Stable Associated Liquid of Short Amyloidogenic Peptides. *Phys. Chem. Chem. Phys.* **2015**, *17*, 10556−10567.

(23) Auer, S.; Ricchiuto, P.; Kashchiev, D. Two-step Nucleation of Amyloid Fibrils: Omnipresent or Not? *J. Mol. Biol.* **2012**, *422*, 723−730.

(24) Matthes, D.; Gapsys, V.; Daebel, V.; de Groot, B. L. Mapping the Conformational Dynamics and Pathways of Spontaneous Steric Zipper Peptide Oligomerization. *PLoS One* **2011**, *6*, e19129.

(25) Li, D.-W.; Mohanty, S.; Irback, A.; Huo, S. Formation and Growth of Oligomers: A Monte Carlo Study of an Amyloid Tau Fragment. *PLoS Comput. Biol.* **2008**, *4*, e1000238.

(26) Morriss-Andrews, A.; Shea, J.-E. Computational Studies of Protein Aggregation: Methods and Applications. *Annu. Rev. Phys. Chem.* **2015**, *66*, 643−666.

(27) Han, W.; Schulten, K. Further Optimization of a Hybrid United-Atom and Coarse-Grained Force Field for Folding Simulations: Improved Backbone Hydration and Interactions between Charged Side Chains. *J. Chem. Theory Comput.* **2012**, *8*, 4413−4424.

(28) Han, W.; Schulten, K. Fibril Elongation by A beta(17−42): Kinetic Network Analysis of Hybrid-Resolution Molecular Dynamics Simulations. *J. Am. Chem. Soc.* **2014**, *136*, 12450−12460.

(29) Bereau, T.; Deserno, M. J. Generic Coarse-Grained Model for Protein Folding and Aggregation. *J. Chem. Phys.* **2009**, *130*, 235106.

(30) Cheon, M.; Chang, I.; Hall, C. K. Influence of Temperature on Formation of Perfect Tau Fragment Fibrils Using PRIME20/DMD Simulations. *Protein Sci.* **2012**, *21*, 1514−1527.

(31) Limbach, H. J.; Arnold, A.; Mann, B. A.; Holm, C. ESPResSo - an Extensible Simulation Package for Research on Soft Matter Systems. *Comput. Phys. Commun.* **2006**, *174*, 704−727.

(32) Arnold, A.; Lenz, O.; Kesselheim, S.; Weeber, R.; Fahrenberger, F.; Roehm, D.; Košovan, P.; Holm, C. *Lect. Notes Comput. Sci. Eng.* **2013**, *89*, 1−23.

(33) Humphrey, W.; Dalke, A.; Schulten, K. VMD: Visual Molecular Dynamics. *J. Mol. Graphics* **1996**, *14*, 33−38.

(34) Sugita, Y.; Okamoto, Y. Replica-Exchange Molecular Dynamics Method for Protein Folding. *Chem. Phys. Lett.* **1999**, *314*, 141−151.

(35) Katzgraber, H. G.; Trebst, S.; Huse, D. A.; Troyer, M. Feedback-optimized parallel tempering Monte Carlo. *J. Stat. Mech.* **2006**, *6*, 1742.

(36) Luiken, J. A.; Bolhuis, P. G. Primary Nucleation Kinetics of Short Fibril-Forming Amyloidogenic Peptides. *J. Phys. Chem. B* **2015**, *119*, 12568−12579.

(37) Seeber, M.; Cecchini, M.; Rao, F.; Settanni, G.; Caflisch, A. Wordom: a Program for Efficient Analysis of Molecular Dynamics Simulations. *Bioinformatics* **2007**, *23*, 2625−2627.

(38) Seeber, M.; Felline, A.; Raimondi, F.; Muff, S.; Friedman, R.; Rao, F.; Caflisch, A.; Fanelli, F. Wordom: A User-Friendly Program for the Analysis of Molecular Structures, Trajectories, and Free Energy Surfaces. *J. Comput. Chem.* **2011**, *32*, 1183−1194.

(39) Ferrenberg, A. M.; Swendsen, R. H. New Monte-Carlo technique for studying phase-transitions. *Phys. Rev. Lett.* **1988**, *61*, 2635.

(40) Dellago, C.; Bolhuis, P. G. Transition Path Sampling and the Calculation of Rate Constants. *J. Chem. Phys.* **1998**, *108*, 1964−1977.

(41) Dellago, C.; Bolhuis, P. G.; Chandler, D. On the Calculation of Reaction Rate Constants in the Transition Path Ensemble. *J. Chem. Phys.* **1999**, *110*, 6617−6625.

(42) Bolhuis, P. G.; Dellago, C.; Geissler, P. L. Transition Path Sampling: Throwing Ropes over Mountains in the Dark. *J. Phys.: Condens. Matter* **2000**, *12*, A147−A152.

(43) Dellago, C.; Bolhuis, P. G.; Geissler, P. L. Transition Path Sampling. *Adv. Chem. Phys.* **2002**, *123*, 1−78.

(44) Bolhuis, P. G.; Chandler, D.; Dellago, C. Transition Path Sampling: Throwing Ropes over Rough Mountain Passes. *Annu. Rev. Phys. Chem.* **2002**, *53*, 291−318.

(45) van Erp, T. S.; Moroni, D.; Bolhuis, P. G. A Novel Path Sampling Method for the Calculation of Rate Constants. *J. Chem. Phys.* **2003**, *118*, 7762−7774.

DOI: 10.1021/acs.jpcb.6b07045
J. Phys. Chem. B 2017, 121, 3250−3261

(46) van Erp, T. S.; Bolhuis, P. G. Elaborating Transition Interface Sampling Methods. *J. Comput. Phys.* **2005**, *205*, 157−181.
(47) Allen, R. J.; Frenkel, D.; ten Wolde, P. R. Simulating Rare Events in Equilibrium or Nonequilibrium Stochastic Systems. *J. Chem. Phys.* **2006**, *124*, 024102.
(48) Kratzer, K.; Berryman, J. T.; Taudt, A.; Zeman, J.; Arnold, A. The Flexible Rare Event Sampling Harness System (FRESHS). *Comput. Phys. Commun.* **2014**, *185*, 1875−1885.
(49) Allen, R. J.; Valeriani, C.; ten Wolde, P. R. Forward Flux Sampling for Rare Event Simulations. *J. Phys.: Condens. Matter* **2009**, *21*, 463102.
(50) Plumley, J. A.; Dannenberg, J. J. Comparison of β-Sheets of Capped Polyalanine with Those of the Tau-Amyloid Structures VQIVYK and VQIINK. A Density Functional Theory Study. *J. Phys. Chem. B* **2011**, *115*, 10560−10566.
(51) von Bergen, M.; Friedhoff, P.; Biernat, J.; Heberle, J.; Mandelkow, E.-M.; Mandelkow, E. Assembly of τ Protein Into Alzheimer Paired Helical Filaments Depends on a Local Sequence Motif (306VQIVYK311) Forming β-Structure. *Proc. Natl. Acad. Sci. U. S. A.* **2000**, *97*, 5129−5134.
(52) Larini, L.; Gessel, M. M.; LaPointe, N. E.; Do, T. D.; Bowers, M. T.; Feinstein, S. C.; Shea, J.-E. Initiation of Assembly of Tau (273−284)and its ΔK280 Mutant: An Experimental and Computational Study. *Phys. Chem. Chem. Phys.* **2013**, *15*, 8916−8928.
(53) Sawaya, M. R.; Sambashivan, S.; Nelson, R.; Ivanova, M. I.; Sievers, S. A.; Apostol, M. I.; Thompson, M. J.; Balbirnie, M.; Wiltzius, J. J. W.; McFarlane, H. T.; et al. Atomic Structures of Amyloid Cross-β Spines Reveal Varied Steric Zippers. *Nature* **2007**, *447*, 453−457.
(54) Zhao, J.-H.; Liu, H.-L.; Chuang, C.-K.; Liu, K.-T.; Tsai, W.-B.; Ho, Y. Molecular Dynamics Simulations to Investigate the Stability and Aggregation Behaviour of the Amyloid-Forming Peptide VQIVYK from Tau Protein. *Mol. Simul.* **2010**, *36*, 1013−1024.
(55) Auer, S.; Dobson, C. M.; Vendruscolo, M.; Maritan, A. Self-Templated Nucleation in Peptide and Protein Aggregation. *Phys. Rev. Lett.* **2008**, *101*, 258101.
(56) Gamblin, T. C.; Berry, R. W.; Binder, L. I. Modeling Tau Polymerization in Vitro: A Review and Synthesis. *Biochemistry* **2003**, *42*, 15009−15017.
(57) Reynolds, M. R.; Berry, R. W.; Binder, L. I. Site-Specific Nitration Differentially Influences τ-Assembly in Vitro. *Biochemistry* **2005**, *44*, 13997−14009.
(58) Riemenschneider, M.; Buch, K.; Schmolke, M.; Kurz, A.; Guder, W. G. Cerebrospinal Protein Tau is Elevated in Early Alzheimer's Disease. *Neurosci. Lett.* **1996**, *212*, 209−211.
(59) Otto, M.; Wiltfang, J.; Tumani, H.; Zerr, I.; Lantsch, M.; Kornhuber, J.; Weber, T.; Kretzschmar, H. A.; Poser, S. Elevated Levels of Tau-Protein in Cerebrospinal Fluid of Patients with Creutzfeldt-Jakob Disease. *Neurosci. Lett.* **1997**, *225*, 210−212.
(60) Green, A. J. E.; Harvey, R. J.; Thompson, E. J.; Rossor, M. N. Increased Tau in the Cerebrospinal Fluid of Patients with Frontotemporal Dementia and Alzheimer's Disease. *Neurosci. Lett.* **1999**, *259*, 133−135.

DOI: 10.1021/acs.jpcb.6b07045
J. Phys. Chem. B 2017, 121, 3250−3261